A Journal of the Gesellschaft Deutscher Chemiker

Angewandte International Edition GDCh Chemie

www.angewandte.org

Accepted Article

Title: A Universal Strategy toward Ultrasmall Hollow Nanostructures with Remarkable Electrochemical Performance

Authors: Minmin Fan, Dankui Liao, Mohamed F. Aly Aboud, Imran Shakir, and Yuxi Xu

To be cited as: *Angew. Chem. Int. Ed.* 10.1002/anie.202000352
Angew. Chem. 10.1002/ange.202000352

Link to VoR: http://dx.doi.org/10.1002/anie.202000352
http://dx.doi.org/10.1002/ange.202000352

WILEY-VCH

10.1002/anie.202000352

WILEY-VCH

RESEARCH ARTICLE

A Universal Strategy toward Ultrasmall Hollow Nanostructures with Remarkable Electrochemical Performance

Minmin Fan,[+a,b] Dankui Liao,[+b] Mohamed F. Aly Aboud,[c] Imran Shakir,[c] and Yuxi Xu*[a]

Abstract: Hollow nanostructures have shown enormous potentials in many fields, but the convenient synthesis of ultrasmall hollow nanostructures with a wide range of compositions remains a considerable challenge. Herein, we report a facile and versatile microwave-assisted and shell-confined Kirkendall diffusion strategy to fabricate a variety of ultrasmall hollow nanoparticles by modulating the growth and thermal conversion of metal-organic framework (MOF) nanocrystals on graphene. Unlike traditional thermal treat route, our method involves that the adsorption of microwave by graphene creates a high-energy environment in a short time to decompose the in-situ grown MOF nanocrystals into well-dispersed uniform core-shell nanoparticles with ultrasmall size rather than large aggregated particles. Upon a newly disclosed shell-confined Kirkendall diffusion process, a series of hollow nanoparticles of multi-metal oxides, phosphides, and sulfides with the diameter below 20 nm and shell thickness below 3 nm can be successfully obtained for the first time. We further revealed that ultrasmall hollow nanostructure such as Fe_2O_3 can promote much faster charge transport and expose more active sites as well as migrate the volume change stress more efficiently than the solid and large hollow counterparts, thus demonstrating remarkable lithium-ion storage performance including ultrahigh reversible capacity (1167 mAh g^{-1} at 0.2 A g^{-1}), excellent rate performance (701 mAh g^{-1} at 5 A g^{-1}) and outstanding cycling stability (97.8% after 1200 cycles at 5 A g^{-1}), which is among the best results reported so far. This study provides an exciting way to design hollow nanostructured functional materials for electrochemical energy storage and beyond.

Introduction

Hollow nanomaterials have attracted growing attention in recent years due to their structure-induced intriguing properties and wide applications, including energy storage, solar cells, catalysis, gas sensors and drug delivery.[1-6] However, the fabrication of hollow nanostructures in a controllable manner remains a considerable challenge.[7,8] To date, there are several developed approaches,[9-11] typically hard/soft-templating and self-templating, to generate hollow nanomaterials. Among them, the Kirkendall effect, which is caused by the differences in diffusion direction and speed between different ions in the synthesis process, is demonstrated to be a simple and effective self-templating method.[12-15] In this regard, with pure bare metal nanoparticles as precursors, liquid-phase injection synthesis and solid-gas reaction have been mostly employed to produce hollow metallic compounds nanostructures.[16-18] For example, hollow $CoSe_2$,[16] Fe_2O_3,[17] Fe_3O_4,[18] Co_9S_8,[19] PdP_2,[20] and Ni_2P[21] nanoparticles were successfully fabricated. However, these preparation methods usually yield relatively large hollow nanoparticles (>40 nm) with single metal components, which suffer from the inefficient large-scale preparation of dispersed/discrete metal nanoparticles and uncontrollable Kirkendall diffusion process.[16,17,20] Therefore, it is essential to develop a new and effective strategy to synthesize ultrasmall hollow nanomaterials with enriched compositions and types for understanding the fundamental structure-property relationship and realizing high-performance applications.[22]

Metal-organic frameworks (MOFs) are a class of inorganic-organic hybrid metal coordination compounds formed by linking inorganic and organic units through coordination bondings.[23,24] Recently, considerable attention has been focused on employing pyrolysis of MOFs as self-sacrificial templates for the synthesis of hollow materials in energy storage because hollow nanoparticles such as oxides, sulfides, and etc. derived from MOFs often exhibit distinct merits such as uniform size, hierarchical porosity, and large surface area.[25,26] However, few hollow materials less than 100 nm have been achieved so far mainly due to the formidable obstacle in controllable synthesis and conversion of ultrasmall MOFs precursors in the whole process.

Herein, we report a universal microwave-assisted and confined-diffusion strategy to fabricate a series of ultrasmall hollow nanoparticles with ultrasmall MOF nanocrystals uniformly grown on graphene as precursors. The adsorption of microwave by graphene creates a high-energy environment to decompose the MOFs nanocrystals into well-dispersed ultrasmall core-shell nanoparticles, and upon a newly disclosed shell-confined Kirkendall diffusion process, ultrasmall hollow nanoparticles can be successfully obtained (Figure 1). Compared with previous work,[27-29] our method possesses several significant features: (i) The MOFs nanocrystals synthesized by our excessive metal ion induced assembly method have an average size below 10 nm and the metal components of MOFs are highly adjustable without any stoichiometry problems. (ii) Unlike traditional thermal treat route, the microwave-assisted process decomposed MOFs into separated metal and carbon/nitrogen-containing gases in seconds rather than aggregated metal and carbon composites, which ensures that the carbon layer can quickly wrap the dispersed metal, resulting in well-dispersed ultrathin carbon encapsulated ultrasmall core-shell nanoparticles. (iii) Interestingly, the carbon shells can not only act as reaction interfaces, but also have a space-limiting effect in the Kirkendall diffusion process,

[a] M. Fan, Prof. Y. Xu
School of Engineering, Westlake University, Hangzhou 310024, Zhejiang Province, China. Institute of Advanced Technology, Westlake Institute for Advanced Study, Hangzhou 310024, Zhejiang Province, China.
E-mail: xuyuxi@westlake.edu.cn (Y. Xu)
[b] M. Fan, Prof. D. Liao
Guangxi Key Laboratory of Petrochemical Resource Processing and Process Intensification Technology, School of Chemistry and Chemical Engineering, Guangxi University, Nanning 530004, China.
[c] Dr. M. Aboud, Prof. I. Shakir
Sustainable Energy Technologies Center, College of Engineering, King Saud University, Riyadh 11421, Kingdom of Saudi Arabia
[+] These authors contributed equally to this work.

Supporting information for this article is given via a link at the end of the document.

10.1002/anie.202000352

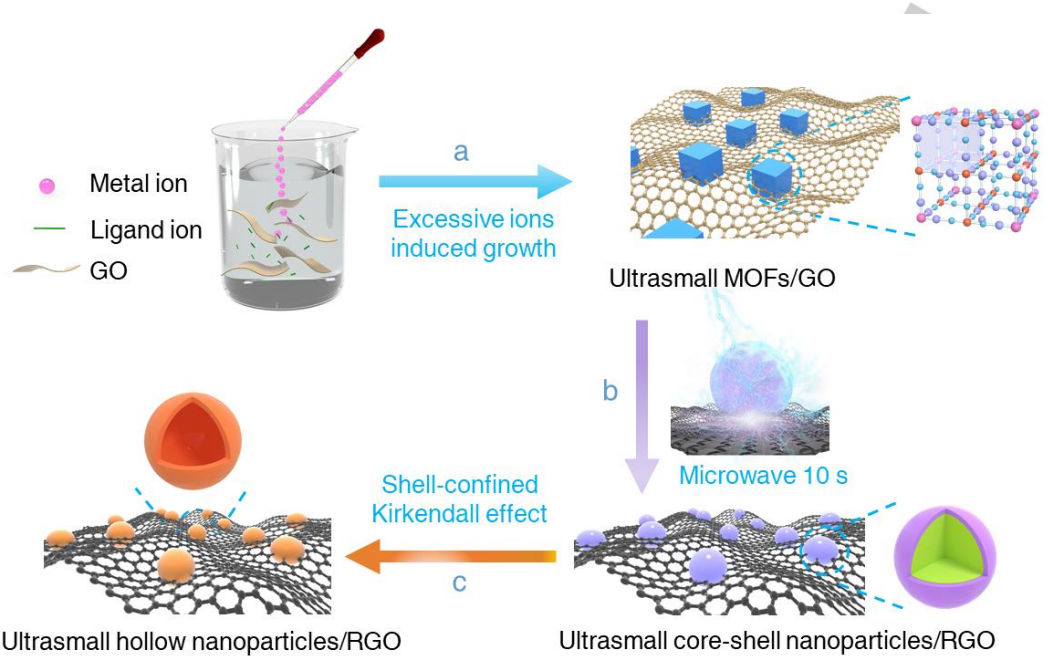

Figure 1. Schematic illustration of the synthesis process of the hollow nanoparticles/RGO. (a) Excessive metal ions induced growth of ultrasmall MOFs nanocrystals on GO. (b) Microwave-assisted rapid synthesis of ultrasmall core-shell nanoparticles on RGO. (c) Shell-confined Kirkendall process for synthesis of ultrasmall hollow nanoparticles on RGO.

which efficiently control the sizes of hollow nanostructures almost same as those of the core-shell nanoparticles precursors and inhibit the fusion of hollow nanostructures. With these features, we can obtain a series of ultrasmall hollow nanomaterials including metal phosphides, metal sulfides, single metal oxides, binary metal oxides, and ternary metal oxides with the smallest diameter down to 10 nm. To the best of our knowledge, there is no report for the preparation of hollow ternary oxides and only very limited binary metal oxides and the diameter of the hollow nanoparticles synthesized by our method is the smallest among the hollow materials synthesized by MOFs as precursors. As a proof of concept, we further reveal that the ultrasmall hollow Fe_2O_3 can promote much faster charge transport and ion diffusion as well as relieve the volume change stress more efficiently than the larger hollow and solid counterparts for the electrochemical reaction, thus demonstrating ultrahigh reversible capacity (1167 mAh g^{-1} at 0.2 A g^{-1} after 110 cycles), excellent rate performance (701 mAh g^{-1} at 5 A g^{-1}) and outstanding cycling stability (97.8% after 1200 cycles at 5 A g^{-1}) as anode for lithium-ion battery, which is among the best reported results.

Results and Discussion

Prussian blue (PB) and prussian blue analogues (PBAs) both are a kind of classical MOFs that could be easily prepared by co-precipitation of metal cations and cyanometallate anions in aqueous solution. The highly tunable metal components as well as the low cost have made PB/PBAs ideal precursors for the fabrication of various functional derivatives. However, the rapid coordination reaction between metal cations and cyanometallate anions usually resulted in large aggregates (Figure S1), which is detrimental to reduce the size of derivatives. We first developed a versatile excessive-metal-ion-induced-assembly method to grow ultrasmall PB/PBA nanoparticles on graphene oxide (GO). Specifically, upon adding excessive metal ions into a homogenous solution of GO and cyanometallate ions, a portion of metal ions reacted with cyanometallate anions to form PB/PBAs and excessive metal ions adsorbed on the surface of PB/PBAs, which promoted the effective deposition of PB/PBAs nanoparticles on GO with oxygen-containing groups by electrostatic and coordination interactions and inhibited the overgrowth of PB/PBAs. As shown in Figure 2a-c, the PB nanoparticles with average size of 5.2 nm were uniformly distributed on GO surface. The Raman spectra (Figure S2a), X-ray diffraction (XRD) (Figure S2b) and Fourier transform infrared spectroscopy (FTIR) (Figure S2c) results confirmed the growth of PB nanoparticles on GO. Meanwhile, other ultrasmall PBAs nanoparticles such as Ni-Ni PBA, Ni–Fe PBA, Fe-Co PBA, and FeNi–Co PBA with sizes below 10 nm can also be obtained by this method (Figure S3 and S4). Here the ultrasmall hollow Fe_2O_3 nanoparticles derived from

10.1002/anie.202000352

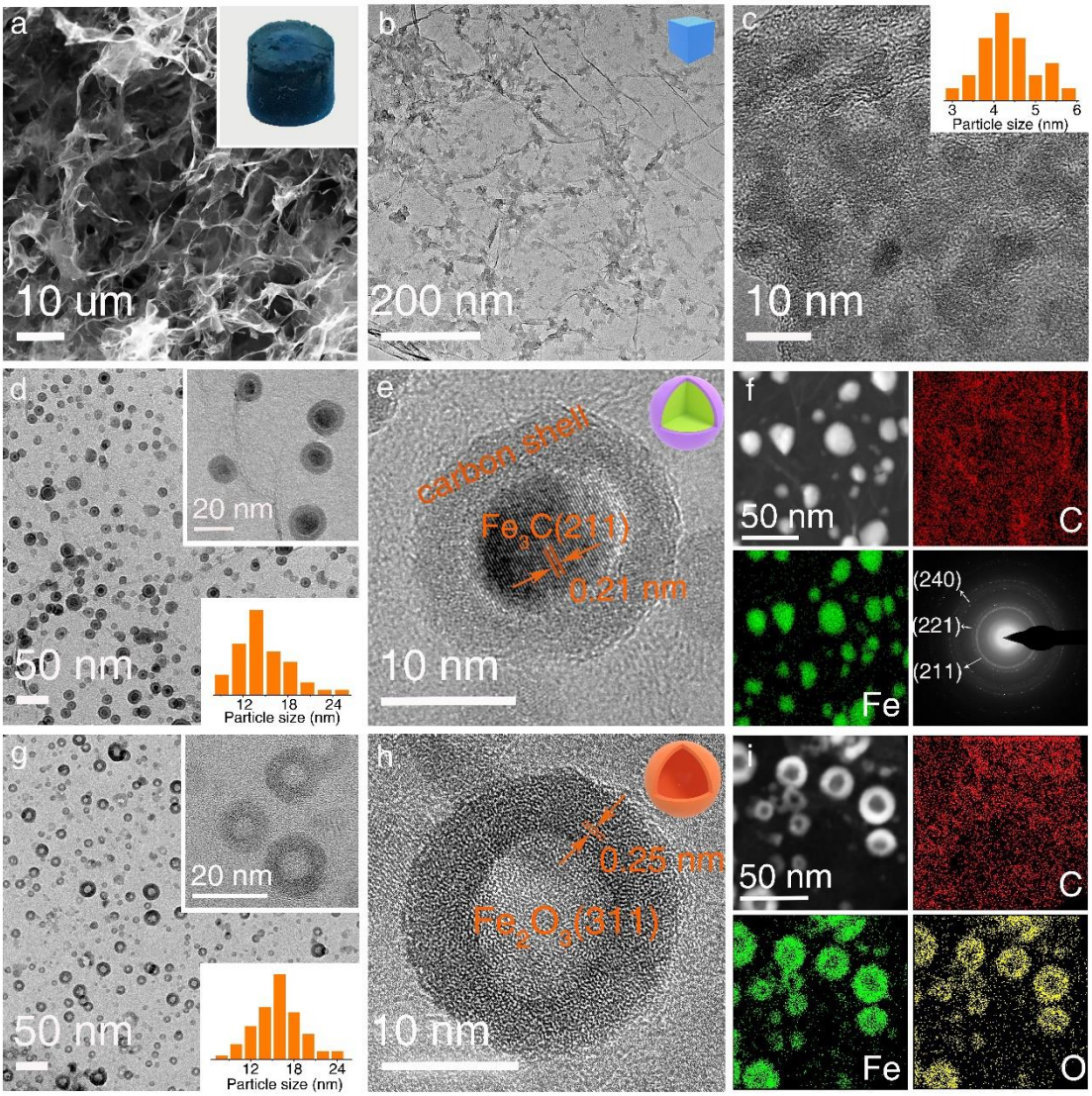

Figure 2. (a) SEM and (b, c) TEM images of the PB/GO aerogel. (d) TEM and (e) HRTEM and (f) STEM image, SAED pattern and element mapping (C, Fe) of Fe_3C@C/RGO. (g) TEM, (h) HRTEM and (i) STEM image and element mapping (C, Fe, O) of S-H-Fe_2O_3/RGO.

PB/GO precursor was chosen as a model to demonstrate our concept firstly. By freeze-drying of the PB/GO dispersion, monolithic aerogel (Figure 2a insert) was obtained and it was further irradiated by microwave under Ar gas. Once the bright spark appeared, the color of PB/GO sponge changed to black immediately within 10 s (Figure S5). As shown in Figure 2d, the original PB nanoparticles were all converted to core-shell nanoparticles with average size of 18 nm and shell thickness of 3 nm, which were evenly distributed on the surface of reduced GO (RGO). The high-resolution transmission electron microscopy (HRTEM) (Figure 2e) and the scanning transmission electron microscopy (STEM) image as well as selected area electron diffraction (SAED) pattern and elemental mappings (Figure 2f) confirmed that the core-shell nanoparticles were Fe_3C@C nanoparticles and well-dispersed on RGO due to the instantaneous reaction process. The Raman (Figure S2a) and XRD (Figure S2b) results also confirmed the decomposition and transformation of PB to Fe_3C@C and the GO was effectively reduced.[30,31] It should be noted that the traditional programmed heating method could not produce such exquisite nanostructure. Upon the programmed heating to 800 ºC for 2 h, the obtained product was large and partially aggregated iron/carbon composite (Fe_xC) nanoparticles with a large average size around 50 nm and without any shells (Figure S6). It could be ascribed to that the adsorption of microwave by graphene created a high-energy environment in a short time to decompose PB into separated metal and carbon/nitrogen-containing gases in the initial stage rather than the aggregated metal/carbon composites presented in

10.1002/anie.202000352

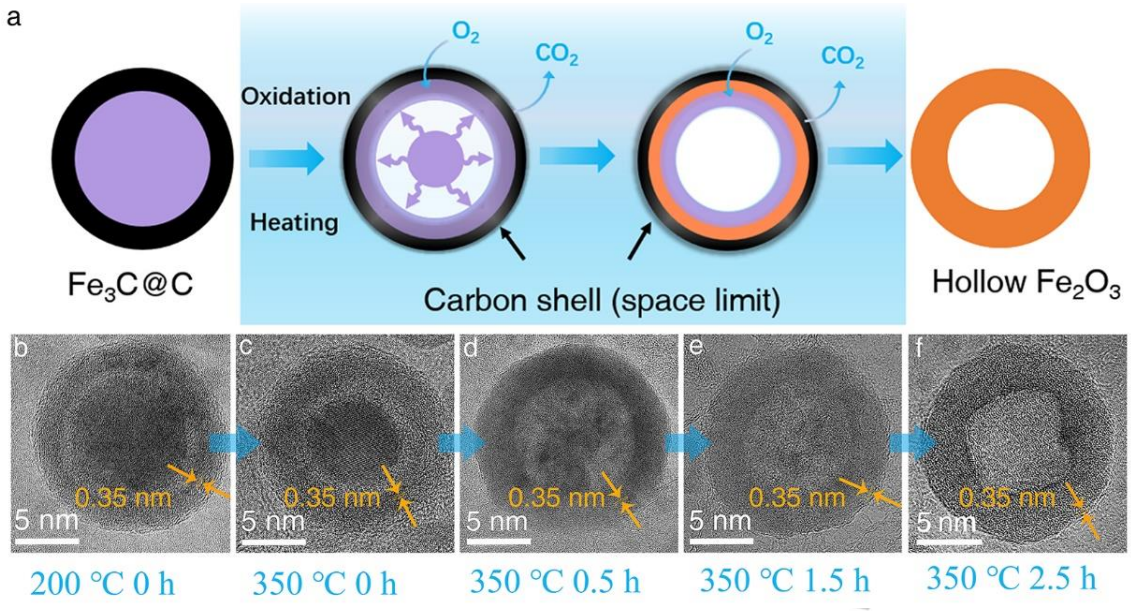

Figure 3. Formation mechanism and conversion process of hollow Fe_2O_3 nanoparticles derived from core-shell Fe_3C@C nanoparticles by the shell-confined Kirkendall diffusion effect (a). The TEM images of the products annealing in the air at different stages of (b) 200 ºC 0 h, (c) 350 ºC 0 h, (d) 350 ºC 0.5 h, (e) 350 ºC 1.5 h, (f) 350 ºC 2.5 h.

traditional programmed heat treatment. Then, the redeposition of carbon-gases enabled the rapid wrapping and isolation of the dispersed metal particles, yielding uniform core-shell nanocrystals with ultrasmall size. This significant difference clearly demonstrated the uniqueness of microwave-assisted process in fabrication of discrete ultrasmall core-shell nanoparticles derived from MOF precursors. In addition, GO could not only facilitate the in-situ growth of ultrasmall PB/PBAs nanoparticles, but also were essential for this ultrafast microwave-assistant reaction due to its functionality of microwave susceptors. The conversion reaction of PB would not happen even after microwave irradiation for 30 min without GO (Figure S7). With the well-dispersed ultrasmall core-shell Fe_3C@C nanoparticles as unique precursors, we could further convert them to ultrasmall hollow Fe_2O_3 nanoparticles through nanoscale Kirkendall effect by simple heating at 350 ºC in air. Interestingly, the hollow Fe_2O_3 nanoparticles were still uniformly dispersed on RGO surface without any aggregation and showed an average size of 18 nm and thickness of 3 nm, almost the same size of the Fe_3C@C nanoparticles (Figure 2g-i). The HRTEM image (Figure 2h) and SAED pattern (Figure S8), as well as Raman (Figure S2a), XRD (Figure S2b) and XPS (Figure S9) results fully confirmed the transformation of Fe_3C@C to Fe_2O_3.

To further understand this conversion process from core-shell Fe_3C@C to hollow Fe_2O_3, we conducted time-dependent experiments. In the typical previous reports of hollow metal oxide,[18,32,33] the oxide interface was first formed on the outside surface of the bare metal nanoparticles. Due to the higher outward diffusion flux of metal compared to inward flux of oxygen, vacancies were created and injected at the oxide interface, and the migration and agglomeration of vacancies finally resulted in the formation of hollow metal oxide. It can be usually observed previously that the size of the product increased significantly and fusion/aggregation happed as the process of Kirkendall diffusion,[20] which was also clearly observed in the oxidation process of the above Fe_xC nanoparticle precursor obtained by traditional programmed heating (Figure S10). Differently, in this study, the outward diffusion of core materials accompanied with the inward diffusion of vacancies from carbon shell to core and the inward diffusion of oxygen along the carbon shell. Subsequently the Fe_3C diffused all the way in the carbon shell and even through the shell and then reacted with oxygen, during which the carbon shell was consumed slowly (Figure 3a). As shown in Figure 3b-f, although the carbon layer with interlayer spacing of 0.35 nm was continuously consumed during the oxidation process, the core was always encapsulated by the carbon layer until the complete formation of hollow Fe_2O_3 nanostructures. We thus proposed that the carbon layer not only act as reaction interfaces for oxygen and iron species, but also acts as a template during the oxidation process, which have a space-limiting effect during the conversion to limit the overgrowth of the size and aggregation of the hollow nanoparticles. If no existence of carbon shells, it is very difficult to manipulate them in air and control the size of the final product. Therefore, the core-shell nanoparticle precursor demonstrated its unique advantage for the fabrication of ultrasmall hollow nanostructures.

This microwave-assisted and shell-confined diffusion method can be easily extended to synthesizing a variety of ultrasmall hollow nanoparticles to meet the need of different applications. With different PBAs/GO precursors discussed above and shown in Figure S3, we can prepare various ultrasmall core-shell nanoparticle intermediates by microwave irradiation (Figure S11)

10.1002/anie.202000352

and further convert them into ultrasmall hollow nanoparticle by shell-confined Kirkendall diffusion such as hollow NiO nanoparticles with average size of 10 nm (Figure 4a1-a7), hollow $FeNiO_x$ nanoparticles with average size of 15 nm (Figure 4b1-b7), hollow $FeCoO_x$ with average size of 17 nm (Figure 4c1-c7) and hollow $FeCoNiO_x$ nanoparticles with average size of 12 nm (Figure 4d1-d7). Furthermore, the hollow FeS_2 nanoparticles with average size of 19 nm (Figure 4e1-e7) and hollow FeP nanoparticles with average size of 21 nm (Figure 4f1-f7) were also obtained by heating the Fe_3C@C/RGO in phosphorus and sulphur atmosphere, respectively. To the best of our knowledge, there is no report for the preparation of hollow ternary oxides and only very limited binary metal oxides and the diameters of the hollow nanoparticles synthesized by this method are the smallest among the hollow materials synthesized with MOFs as precursors.

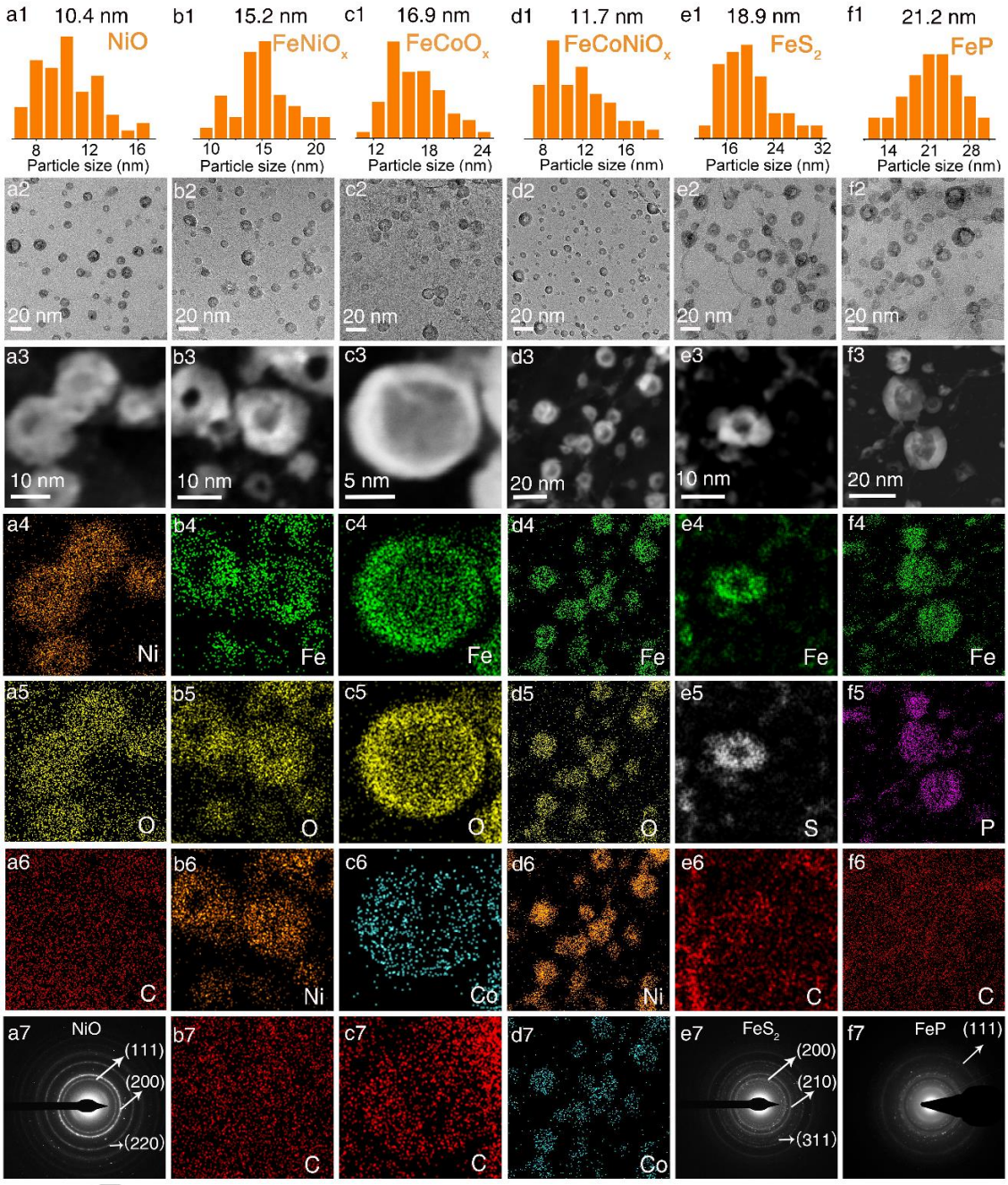

Figure 4. Controllable synthesis of hollow nanoparticles with different components. (a1-f1) Particle size distribution, (a2-f2) TEM images, (a3-f3) STEM images, and (a4-f4, a5-f5, a6-f6) EDS mapping images, and (a7-f7) SAED images and EDS mapping images.

10.1002/anie.202000352

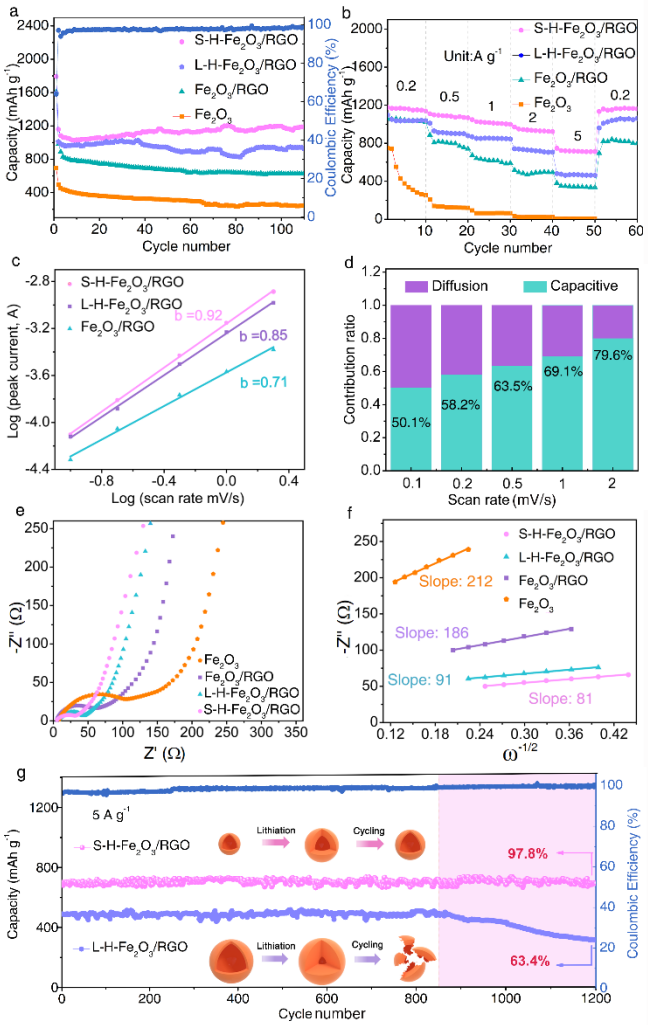

Figure 5. Electrochemical characterizations of S-H-Fe_2O_3/RGO, L-H-Fe_2O_3/RGO, Fe_2O_3/RGO, and Fe_2O_3 anodes. (a) cycling performance of S-H-Fe_2O_3/RGO, L-H-Fe_2O_3/RGO, Fe_2O_3/RGO, and Fe_2O_3 anodes at 0.2 A g^{-1}; (b) rate performance of S-H-Fe_2O_3/RGO, L-H-Fe_2O_3/RGO, Fe_2O_3/RGO, and Fe_2O_3 anodes; (c) *b* values of S-H-Fe_2O_3/RGO, L-H-Fe_2O_3/RGO, and Fe_2O_3/RGO at scan rates from 0.1-2 mV s^{-1}; (d) contribution ratio of capacitive- and diffusion-controlled capacities at different scan rates for S-H-Fe_2O_3/RGO; (e) EIS plots and (f) the linear fitting of Z′ versus $\omega^{-1/2}$ for S-H-Fe_2O_3/RGO, L-H-Fe_2O_3/RGO, Fe_2O_3/RGO, and Fe_2O_3 anodes; (g) cycling performance of S-H-Fe_2O_3/RGO and L-H-Fe_2O_3/RGO at 5 A g^{-1} for 1200 cycles.

The hollow nanostructures have demonstrated great potentials in electrochemical energy storage and conversion. However, the performance is still need to improve and the understanding of size effect remains scarce. As a proof of concept, we studied the electrochemical performance of ultrasmall hollow Fe_2O_3 nanoparticle on RGO (S-H-Fe_2O_3/RGO) composite as representative anode for lithium-ion battery. For comparison, we also fabricated the large hollow Fe_2O_3 nanoparticle/RGO composite (L-H-Fe_2O_3/RGO) with an average size of 50 nm, which is typical size in previous studies (Figure S12),[34-38] and the solid Fe_2O_3 nanoparticles/RGO composite (Fe_2O_3/RGO) with an average size of 50 nm (Figure S13). Due to the robust 3D porous graphene network, the H-Fe_2O_3/RGO, L-H-Fe_2O_3/RGO and Fe_2O_3/RGO composite aerogels could be easily compresses into compact flexible films and used as binder-free anodes to assemble the cells (Figure S14). The weight content of Fe_2O_3 in the H-Fe_2O_3/RGO, L-H-Fe_2O_3/RGO and Fe_2O_3/RGO composite all were nearly to be 57 wt% based on the thermogravimetric analysis (TGA) (Figure S15).

The typical galvanostatic discharge-charge curves of S-H-Fe_2O_3/RGO at 0.2 A g^{-1} between 0.01 and 3 V (versus Li/Li^+) showed two voltage plateaus at 1.5 and 0.9 V in the first discharge curve and one voltage plateau at 1.25 V in the first discharge curve with initial discharge/charge capacities of 1794/1163 mAh g^{-1} at 0.2 A g^{-1}, which can be ascribed to the electrochemical reactions between Fe_2O_3 and Li^+ (Fe_2O_3 → $Li_xFe_2O_3$ → cubic $Li_2Fe_2O_3$ ↔ Fe + Li_2O) and formation of solid electrolyte interface (Figure S16a).[37,38] When cycling at low current density, the L-H-Fe_2O_3/RGO, Fe_2O_3/RGO and pure Fe_2O_3 all showed capacity decay with different levels, while the S-H-Fe_2O_3/RGO anodes delivered a stable and ultrahigh reversible capacity of 1167 mAh g^{-1} after 110 cycles, much higher than that of the L-H-Fe_2O_3/RGO (898 mAh g^{-1}), the Fe_2O_3/RGO (689 mAh g^{-1}) and the pure Fe_2O_3 (180 mAh g^{-1}) (Figure 5a), indicating the superior structural stability and higher electrochemical activity of the ultrasmall hollow Fe_2O_3 nanoparticles. The increasing trend of the capacity of S-H-Fe_2O_3/RGO at 0.2 A g^{-1} mainly derive from the gradual activation process of the electrode materials, which has also been observed in other metal oxide materials.[39-41] The rate performances of these electrode materials were further tested. As shown in Figure 5b and Figure S16b, the S-H-Fe_2O_3/RGO delivered an excellent rate capability with highly reversible capacities of 1167, 1087, 1012, 936, and 701 mAh g^{-1} at 0.2, 0.5, 1, 2, and 5 A g^{-1}, respectively, much better than those of L-H-Fe_2O_3/RGO, Fe_2O_3/RGO, and pure Fe_2O_3.

To understand the superior electrochemical performance of ultrasmall hollow nanostructures, we have performed CV at different scan rates (0.1-2 mV s^{-1}) to analyze the reaction kinetics for the S-H-Fe_2O_3/RGO (Figure S17), L-H-Fe_2O_3/RGO (Figure S18), and Fe_2O_3/RGO (Figure S19) based on the following relationship: $i_p = \alpha v^b$, where i_p and v are peak current and scan rate, respectively, while a and *b* are variables, with the *b*-value determined from the slope of the plot of log i_p versus log v. A *b* value of 0.5 indicates that the electrochemical process is diffusion-limited behavior, when b=1.0, it indicates a surface-controlled capacitive process.[42-47] The *b* value of the S-H-Fe_2O_3/RGO was calculated to be 0.92 at scan rates from 0.1 to 2 mV s^{-1}, higher than that of the L-H-Fe_2O_3/RGO (0.85) and the Fe_2O_3/RGO (0.71) (Figure 5c), demonstrating more dominant surface-controlled kinetics for the S-H-Fe_2O_3/RGO and in accordance with its remarkable rate performance.

To further quantify the surface-capacitive and diffusion-limited contributions to the total capacity, a closer examination of the voltammetric sweep rate dependence was performed according to the following this equation: $i(V) = k_1v + k_2v^{1/2}$, where $i(V)$ is the current at a given potential, and k_1v and $k_2v^{1/2}$correspond to the

10.1002/anie.202000352

current contributions from the surface-capacitive effect and the diffusion-controlled process, respectively. As shown in Figure 5d, the normalized contribution rate of capacitive-controlled capacity at 0.1 mV s^{-1} was about 50% for S-H-Fe_2O_3/RGO, and this value gradually boosted to nearly 80% at 2 mV s^{-1} (Figure 5d), which was higher than those of L-H-Fe_2O_3/RGO and the Fe_2O_3/RGO (Figure S18 and S19). Such a large contribution from capacitive lithium storage not only endows the S-H-Fe_2O_3/RGO anode with an excellent high-rate capability but also an improved cycling performance at high rates.[38,48]

The electrochemical process of S-H-Fe_2O_3/RGO, L-H-Fe_2O_3/RGO, Fe_2O_3/RGO, and pure Fe_2O_3 electrodes were further investigated by the electrochemical impedance spectroscopy (EIS). As show in Figure 5e, both the charge-transfer resistance in the high- to medium-frequency region and Warburg impedance in the low-frequency region of S-H-Fe_2O_3/RGO were smaller than those of L-H-Fe_2O_3/RGO, Fe_2O_3/RGO, and pure Fe_2O_3. Moreover, the lithium diffusion coefficients of different electrodes were evaluated using the follow equation: $D_{Li^+} = 0.5(RT/AF^2\sigma_w C)^2$, where R, T, A, and F are the gas constant, absolute temperature, surface area of the anode and Faraday constant, respectively. C is the concentration of lithium ion, and Warburg coefficient is represented by σ_w, which is related to Z' in equation: $Z' = R_e + R_{ct} + \sigma_w \omega^{-1/2}$, where low frequency region is represented by ω, R_e, and R_{ct} are kinetics parameters independent of frequency, and plot of Z' versus the reciprocal square root of the lower angular frequencies ($\omega^{-1/2}$) is represented by σ_w.[49] The Warburg coefficients (σ_w) of the S-H-Fe_2O_3/RGO, L-H-Fe_2O_3/RGO, Fe_2O_3/RGO, and Fe_2O_3 were calculated to be 81, 91, 186, and 212 Ω $s^{-1/2}$, respectively (Figure 5f). Because the D_{Li^+} is inversely proportional to the σ_w value, the ultrasmall hollow nanostructure with the smallest σ_w value favored the fastest Li^+ diffusion rate, which was consistent with galvanostatic intermittent titration technique results (Figure S20) and accounted for the excellent electrochemical performance of S-H-Fe_2O_3/RGO.

To further assess the long-term cycling stability of electrodes at high rates, the S-H-Fe_2O_3/RGO, L-H-Fe_2O_3/RGO and Fe_2O_3/RGO were tested at 5 A g^{-1}. Remarkably, the H-Fe_2O_3/RGO exhibited a reversible capacity of 684 mAh g^{-1} with an ultrahigh capacity retention of 97.8% even after 1200 cycles. In contrast, although the L-H-Fe_2O_3/RGO maintained stable capacity in the initial stage, it began to show obvious capacity decay after 850 cycles (Figure 5g), which was neglected in previous studies.[3,7] Besides, the Fe_2O_3/RGO shows the worst cycling stability with a capacity retention of 48.4% after 1000 cycles (Figure S21). This significant difference can be ascribed to the different stress migration ability of these electrodes towards the volume fluctuation during the charge-discharge process, which was confirmed by the TEM images (Figure S22). The morphology of ultrasmall hollow Fe_2O_3 nanoparticles in the S-H-Fe_2O_3/RGO electrode remained largely unchanged after 1200 cycles at 5 A g^{-1} (Figure S22a, b), while the large hollow Fe_2O_3 nanoparticles in the L-H-Fe_2O_3/RGO broke into small pieces (Figure S22c, d). It should be noted that the capacity and rate performance of the S-H-Fe_2O_3/RGO anode are higher than most Fe_2O_3-based and other metal oxide-based anodes for LIBs reported thus far (Table S1, S2).

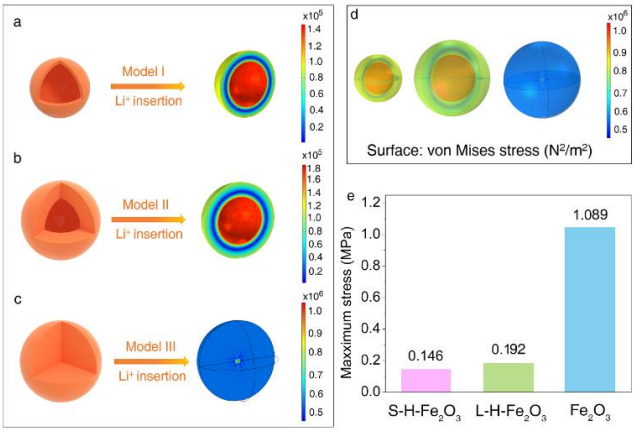

Figure 6. Cross-sectional stress contours and stress colormap of (a) S-H-Fe_2O_3, (b) L-H-Fe_2O_3, and (c) Fe_2O_3. (d) The surface stress contours and (e) comparison of maximum stress of S-H-Fe_2O_3, L-H-Fe_2O_3, and Fe_2O_3.

To shed light on the stress response of the electrodes during lithiation, we modelled the von Mises stress contours for three representative Fe_2O_3 nanoparticles, i.e., the small hollow sphere (18 nm), the large hollow sphere (50 nm), and the large solid sphere (50 nm), under an isotropic initial stress by the finite element method (Figure 6) (detailed information see methods of Supporting Information and Figure S23). The correlation between particle morphology and the electrochemical properties of LIBs is established from the perspective of micromechanics. Figure 6a-d depict the obtained von Mises stress contours and the stress colormap of the three models. The maximum stress of the S-H-Fe_2O_3, L-H-Fe_2O_3, and solid Fe_2O_3 during Li^+ insertion is 0.146 Mpa, 0.192 Mpa, and 1.089 Mpa, respectively (Figure 6e), suggesting that the hollow structure with ultrasmall size alleviated the stress accumulation process and fostered the relaxation of stress, resulting in better cycling stability.

Conclusion

In summary, we have developed a versatile methodology to fabricate ultrasmall hollow nanostructure with MOF nanocrystals on graphene as unique precursors. This strategy involves the controllable growth of MOF nanocrystals on graphene, microwave-assisted conversion of MOF nanocrystals into core-shell nanoparticles, and shell-confined Kirkendall diffusion process, all of which play important role in achieving the ultrasmall hollow nanostructures. With highly adjustable components of PB/PBA MOFs in this study, we can obtain a series of ultrasmall hollow nanomaterials including metal phosphides, metal sulfides, single metal oxides, binary metal oxides, and ternary metal oxides with the typical sizes below 20 nm, which has never been achieved before. Based on this method, it is possible that fabricate hollow structures with desirable compositions and sizes

for various requirements. We further reveal experimentally and theoretically that the ultrasmall hollow nanostructure can promote much faster charge transport and more efficient alleviation of the volume change stress than the solid and large hollow counterparts, thus realizing ultrahigh electrochemical performance. We believe this study provides an exciting way to synthesize ultrasmall hollow nanostructured functional materials for highly efficient electrochemical energy storage and beyond.

Acknowledgements

We acknowledge the support by the National Natural Science Foundation of China (51873039, 51673042), the Young Elite Scientist Sponsorship Program by CAST (2017QNRC001), and the Open Project of Guangxi Key Laboratory of Petrochemical Resource Processing and Process Intensification Technology (2018K006, 2019K002). We extend our sincere appreciation to the Deanship of Scientific Research at King Saud University for its funding of this research through the Research Group Project no RGP-VPP-312.

Keywords: hollow nanostructure • ultrasmall size effect• microwave-assisted • shell-confined Kirkendall effect • lithium-ion battery

[1] L. Yu, X. Y. Yu, X. W. D. Lou, *Adv. Mater.* **2018**, *30*, 1800939.
[2] J. Wang, Y. Cui, D. Wang, *Adv. Mater.* **2018**, *31*, 1801993.
[3] J. Feng, Y. Yin, *Adv. Mater.* **2018**, *31*, 1802349.
[4] J. Wang, J. Wan, D. Wang, *Acc. Chem. Res*. **2019**, *52*, 2169-2178.
[5] J. Wang, H. Tang, L. Zhang, H. Ren, R. Yu, Q. Jin, J. Qi, D. Mao, M. Yang, Y. Wang, P. Liu, Y. Zhang, Y. Wen, L. Gu, G. Ma, Z. Su, Z. Tang, H. Zhao, D. Wang, *Nat. Energy* **2016**, *1*, 16050.
[6] J. Wang, H. Tang, H. Wang, R. Yu, D. Wang, *Mater. Chem. Front.* **2017**, *1*, 414-430.
[7] H. Tabassum, R. Zou, A. Mahmood, Z. Liang, Q. Wang, H. Zhang, S. Gao, C. Qu, W. Guo, S. Guo, *Adv. Mater.* **2018**, *30*, 1705441.
[8] X. Gao, G. Li, Y. Xu, Z. Hong, C. Liang, Z. Lin, *Adv. Mater.* **2008**, *13*, 2622-2627.
[9] D. Mao, J. Wan, J. Wang, D. Wang, *Adv. Mater*. **2019**, *31*, 1802874.
[10] J. Zhang, H. Ren, J. Wang, J. Qi, R. Yu, D. Wang, Y. Liu, *J. Mater. Chem. A*, **2016**, *4*, 17673-17677.
[11] H. Ren, J. Sun, R. Yu, M. Yang, L. Gu, P. Liu, D. Wang, *Chem. Sci*. **2016**, *7*, 793-798.
[12] L. Zhou, Z. Zhuang, H. Zhao, M. Lin, D. Zhao, L. Mai, *Adv. Mater.* **2017**, *29*, 1602914.
[13] Y. Son, M. Choi, M. Ko, S. Chae, N. Park, J. Cho, *Nano Lett.* **2015**, *15*, 6914-6918.
[14] J. S. Cho, Y. C. Kang, *Small* **2015**, *11*, 4673-4681.
[15] Y. Zhao, X. Li, B. Yan, D. Xiong, D. Li, S. Lawes, X. Sun, *Adv. Energy Mater.* **2016**, *6*, 1502175.
[16] Y. Yin, R. M. Rioux, C. K. Erdonmez, S. Hughes, G. A. Somorjai, A. P. Alivisatos, *Science* **2004**, *304*, 711-714.
[17] A. Cabot, V. F. Puntes, E. Shevchenko, Y. Yin, L. Balcells, M. A. Marcus, S. M. Hughes, A. P. Alivisatos, *J. Am. Chem. Soc.* **2007**, *129*, 10358-10360.
[18] S. Peng, S. Sun, *Angew. Chem. Int. Ed.* **2007**, *46*, 4155-4158.
[19] Y. Yin, C. K. Erdonmez, A. Cabot, S. Hughes, A. P. Alivisatos, *Adv. Funct. Mater.* **2006**, *16*, 1389-1399.
[20] H. Tianou, W. Wang, X. Yang, Z. Cao, Q. Kuang, Z. Wang, Z. Shan, M. Jin, Y. Yin, *Nat. Commun.* **2017**, *8*, 1261.
[21] R. K. Chiang, R. T. Chiang, *Inorg. Chem.* **2007**, *46*, 369-371.
[22] F. Yan, D. Guo, S. Zhang, C. Li, C. Zhu, X. Zhang, Y. Chen, *Nanoscale* **2018**, *10*, 2697-2703.
[23] S. Dang, Q. L. Zhu, Q. Xu, *Nat. Rev. Mater.***2017**, *3*, 17075.
[24] S. Wu, J. Liu, H. Wang, H. Yan, *Inte. J. Energy Res.* **2019**, *43*, 697-716.
[25] Y. Li, J. Hu, K. Yang, B. Cao, Z. Li, L. Yang, F. Pan, *Mater. Today Energy* **2019**, *14*, 100332.
[26] J. Zhang, J. Wan, J. Wang, H. Ren, R. Yu, L. Gu, Y. Liu, S. Feng, D. Wang, *Angew. Chem*. *Int. Ed.* **2019**, *58*, 5266-5271.
[27] J. Nai, X. W. D. Lou, *Adv. Mater.* **2019**, *31*, 1706825.
[28] X. Wang, L. Yu, B. Y. Guan, S. Song, X. W. Lou, *Adv. Mater.* **2018**, *30*, 1801211.
[29] A. Indra, T. Song, U. Paik, *Adv. Mater.* **2018**, *30*, 1705146.
[30] Y. Hou, T. Huang, Z. Wen, S. Mao, S. Cui, J. Chen, *Adv. Energy Mater.* **2014**, *4*, 1400337-1400343
[31] W. Jiang, L. Gu, L. Li, Y. Zhang, X. Zhang, L. Zhang, L. Wan, *J. Am. Chem. Soc. 2016, 138, 3570-3578*
[32] W. Weng, J. Lin, Y. Du, X. Ge, X. Zhou, J. Bao, *J. Mater. Chem. A* **2018**, *6*, 10168-10175.
[33] J. Zhou, H. Song, X. Chen, L. Zhi, J. Huo, B. Cheng, *Chem. Mater.* **2009**, *21*, 3730-3737.
[34] H. Sun, G. Xin, T. Hu, M. Yu, D. Shao, X. Sun, J. Lian, *Nat. Commun.* **2014**, *5*, 4526.
[35] Z. Wang, L. Zhou, X. W. Lou, *Adv. Mater.* **2012**, *24*, 1903-1911.
[36] L. Zhang, H. B. Wu, S. Madhavi, H. H. Hng, X. W. Lou, *J. Am. Chem. Soc.* **2012**, *134*, 17388-17391.
[37] Z. H. Chen, J. D. Chen, F. X. Bu, P.O. Agboola, I. Shakir, Y. X. Xu, *ACS Nano* **2018**, *12*, 12879-12887.
[38] P. T. Xiao, F. X. Bu, R. Zhao, M. F. Aly Aboud, I. Shakir, Y. X. Xu, *ACS Nano* **2018**, *12*, 3947-3953.
[39] W. Wei, S. Yang, H. Zhou, I. Lieberwirth, X. Feng, K. Mullen, *Adv. Mater. **2013**, 25, 2909-2914*.
[40] C. Peng, B. Chen, Y. Qin, S. Yang, C. Li, Y. Zuo, J. Yang, *ACS Nano* **2012**, *6*, 1074-1081.
[41] J. S. Do, C. H. Weng, *J. Power Sources* **2005**, *146*, 482-486.
[42] X. Cao, B. Zheng, X. Rui, W. Shi, Q. Yan, H. Zhang, *Angew. Chem. Int. Ed.* **2014**, *53*, 1404-1409.
[43] P. Lou, Z. Cui, Z. Jia, J. Sun, Y. Tan, X. Guo, *ASC Nano* **2017**, *11*, 3705-3715.
[44] J. Sun, C. Lv, F. Lv, S. Chen, D. Li, Z. Guo, W. Han, D. Yang, S. Guo, *ACS Nano* **2017**, *11*, 6186-6193.
[45] Y. Liu, Z. Sun, X. Sun, Y. Lin, K. Tan, J. Sun, L. Liang, L. Hou, C. Yuan, *Angew. Chem. Int. Ed.* 2020, *59*, 2473-2482.
[46] Z. Wang, D. K. Denis, Z. Zhao, X. Sun, J. Zhang, L. Hou, C. Yuan, *J. Mater. Chem. A.* **2019**,*7*, 18109-18117.
[47] Y. Liu, Y. J. Fang, Z. Zhao, C. Yuan, X. W. Lou, *Adv. Energy Mater*. **2019**, *9*, 1803052.
[48] D. Lin, Y. Liu, Y. Li, Y. Li, A. Pei, J. Xie, W. Huang, Y. Cui, *Nat. Chem.* **2019**, *11*, 382.
[49] C. An, Y. Yuan, B. Zhang, L. Tang, B. Xiao, Z. He, J. Zheng, J. Lu, *Adv. Energy Mater.* **2019**, *9*, 1900356.

10.1002/anie.202000352

WILEY-VCH

RESEARCH ARTICLE

Entry for the Table of Contents

RESEARCH ARTICLE

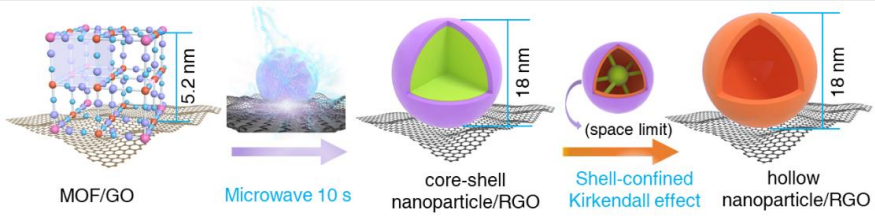

*Minmin Fan, Dankui Liao, Mohamed F. Aly Aboud, Imran Shakir, and Yuxi Xu**

Page No. – Page No.

A Universal Strategy toward Ultrasmall Hollow Nanostructures with Remarkable Electrochemical Performance

[a] M. Fan, Y. Xu
School of Engineering
Westlake University, Hangzhou 310024, China.
E-mail: xuyuxi@westlake.edu.cn
[b] M. Fan, D. L
Guangxi Key Laboratory of Petrochemical Resource Processing and Process Intensification Technology
School of Chemistry and Chemical Engineering